


## Ice microphysical processes exert a strong control on the simulated radiative energy budget in the tropics

Sylvia C. Sullivan<sup>1</sup>  & Aiko Voigt<sup>2,3</sup> 

Simulations of the global climate system at storm-resolving resolutions of 2 km are now becoming feasible and show promising realism in clouds and precipitation. However, shortcomings in their representation of microscale processes, like the interaction of cloud droplets and ice crystals with radiation, can still restrict their utility. Here, we illustrate how changes to the ice microphysics scheme dramatically alter both the vertical profile of cloud-radiative heating and top-of-atmosphere outgoing longwave radiation (terrestrial infrared cooling) in storm-resolving simulations over the Asian monsoon region. Poorly-constrained parameters in the ice nucleation scheme, overactive conversion of ice to snow, and inconsistent treatment of ice crystal effective radius between microphysics and radiation alter cloud-radiative heating by a factor of four and domain-mean infrared cooling by  $30 \text{ W m}^{-2}$ . Vertical resolution, on the other hand, has a very limited impact. Even in state-of-the-art models then, uncertainties in microscale cloud properties exert a strong control on the radiative budget that propagates to both atmospheric circulation and regional climate. These uncertainties need to be reduced to realize the full potential of storm-resolving models.

<sup>1</sup>Institute of Meteorology and Climate Research, Karlsruhe Institute of Technology, Karlsruhe, Germany. <sup>2</sup>Department of Meteorology and Geophysics, University of Vienna, Vienna, Austria. <sup>3</sup>Lamont-Doherty Earth Observatory, Columbia University, New York City, NY, USA. email: [sylvia.sullivan@kit.edu](mailto:sylvia.sullivan@kit.edu); [aiko.voigt@univie.ac.at](mailto:aiko.voigt@univie.ac.at)

Storm-resolving atmospheric simulations have become computationally feasible over large domains and long time periods in recent years and now represent the forefront of global modeling<sup>1,2</sup>. Also called convection-permitting or cloud-resolving models, these models employ fine-enough spatial meshes (5-km or less) to resolve deep convective plumes, thereby circumventing the persistent challenge of convective parameterization. Shallow convection remains parameterized, as the turbulent updrafts from which it initiates may extend over only tens of meters. These models generate more realistic spatial fields of vertical motion, cloud condensate, and precipitation and improve tropical cyclogenesis and the diurnal cycle of precipitation relative to coarser resolution models<sup>1,3,4</sup>. Despite these promising results, subgrid-scale processes like cloud microphysics must still be represented approximately in these models, and associated uncertainties propagate to large-scale values like the atmospheric stability or cloud feedback parameters. Within cloud microphysics, the ice phase is notoriously complicated to represent, for example because of ice crystal non-sphericity and the diversity of atmospheric ice-nucleating particles<sup>5–7</sup>. The challenge of representing ice microphysics contributes to the large spread in the response of tropical anvil cloud coverage to climate warming, now the most uncertain among cloud feedbacks<sup>8</sup>. Thus, ice clouds may become a primary roadblock in the era of storm-resolving modeling, and here, we target their impact on the radiative budget of the Asian monsoon region, a key area for the global climate system<sup>9,10</sup>.

Ice clouds both reflect incoming ultraviolet radiation and absorb and reemit outgoing infrared radiation, generating a dipole of in-cloud heating and cloud-top cooling<sup>11,12</sup>. In the tropics, where ice cloud coverage can be up to 70%<sup>13</sup>, this infrared absorption strongly influences the present-day, large-scale circulation in a variety of ways, for example tightening the region of tropical ascent and strengthening the Northern Hemisphere jet stream<sup>14–16</sup>. Absorption by ice clouds will also partially determine how large-scale circulation responds to global warming. Ice cloud formation, and hence absorption, occurs at higher altitudes in a warmer climate, intensifying the equator-to-pole temperature gradient and pushing the zonal-mean mid-latitude circulation poleward<sup>17,18</sup>. This robust lifting of ice clouds means that we can link the cloud-radiative heating profiles in present-day climate to those in a warmer climate and, in turn, to constraints on the circulation response to future warming<sup>18,19</sup>.

Currently, upper-tropospheric cloud-radiative heating rates vary dramatically from one model to another and between models and satellite data, especially in the tropics<sup>16,18,20</sup>. Here, we test the hypothesis that this variability results from our assumptions about the ice phase in clouds, or ice microphysics. When we no longer parameterize deep convection in storm-resolving simulations, the vertical velocity distribution to which ice formation is highly sensitive improves<sup>21,22</sup>, but uncertainties in ice crystal numbers, sizes, and shapes will persist. We provide initial estimates for how much cloud-radiative heating can vary with these ice microphysical properties.

## Results

**Variations in tropical cloud-radiative heating.** We begin by illustrating the range in tropical-mean profiles of upper-tropospheric cloud-radiative heating ( $\mathcal{H}$ ), produced by three different global coarse-resolution simulations and from CloudSat/CALIPSO measurements (see “Methods”). These  $\mathcal{H}$  profiles can be interpreted as a tropical climatology from models equivalent to those of the Coupled Model Intercomparison Project (CMIP). The profile shapes and values are vastly different from one model to another (Fig. 1a): Maximum  $\mathcal{H}$  varies by a factor of two, from 0.4 K day<sup>-1</sup> up to 1 K day<sup>-1</sup>, as does the vertical depth over which this heating occurs, from 200 hPa to 400 hPa. The CloudSat/CALIPSO data gives yet another picture with multiple heating maxima, all below 0.4 K day<sup>-1</sup>. Importantly, the tropical-mean heating is mirrored quite well by that in our Asian monsoon simulation domain (dashed lines, Fig. 1a), indicating the utility of this region to understand variability in tropical  $\mathcal{H}$  more broadly.

To determine whether we can generate the same diversity in  $\mathcal{H}$  from convection-permitting simulations, we run 2.5-km-equivalent resolution simulations with the Icosahedral Nonhydrostatic (ICON) model over the Asian monsoon region during August 2017 with two different vertical resolutions and a variety of ice microphysical settings (Fig. 1b, c). We switch from one-moment microphysics in which only ice mass is tracked to two-moment microphysics in which both ice mass and number are tracked. We also adjust vertical resolution, include aerosol dependence, and make the formulation of ice crystal effective radius ( $r_{ei}$ ) consistent between the microphysics and radiation schemes (Table S1). By default, the ice crystal effective radius depends only on ice mass,

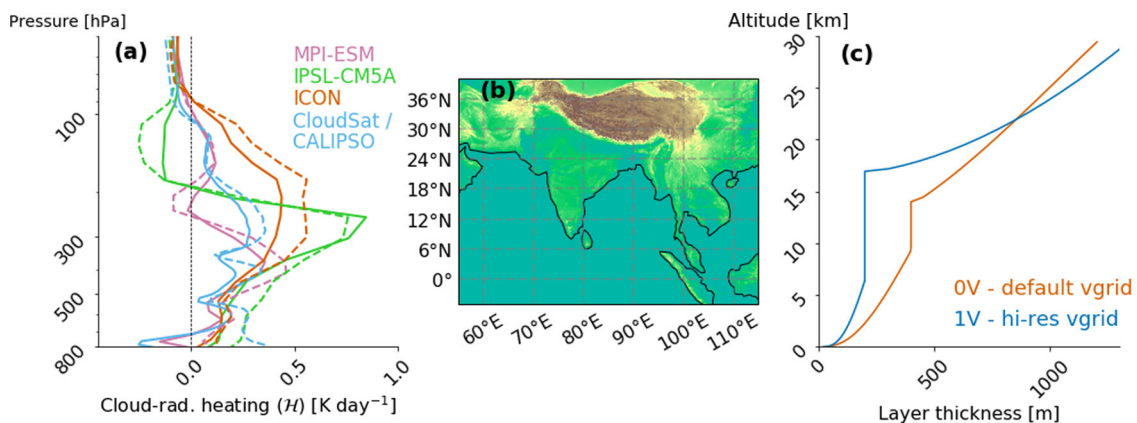


**Fig. 1 Tropics-mean upper-tropospheric  $\mathcal{H}$  varies quantitatively and qualitatively between models and measurements and is well-represented by that of the Asian monsoon region.** Multi-year mean cloud-radiative heating profiles from the MPI-ESM, IPSL-CM5A, and ICON models, as well as 2B-FLXHR-LIDAR data from CloudSat/CALIPSO are shown for the tropics (30°S to 30°N) in solid lines and for the Asian monsoon simulation domain in dashed lines (a). The simulation domain covers the Asian monsoon region from 5°S to 40°N and 55°E to 115°E (b). In our high vertical resolution simulations, the minimum vertical level spacing below 17 km is held to 200 m for a total of 120 model levels, relative to the default 75 levels (c).

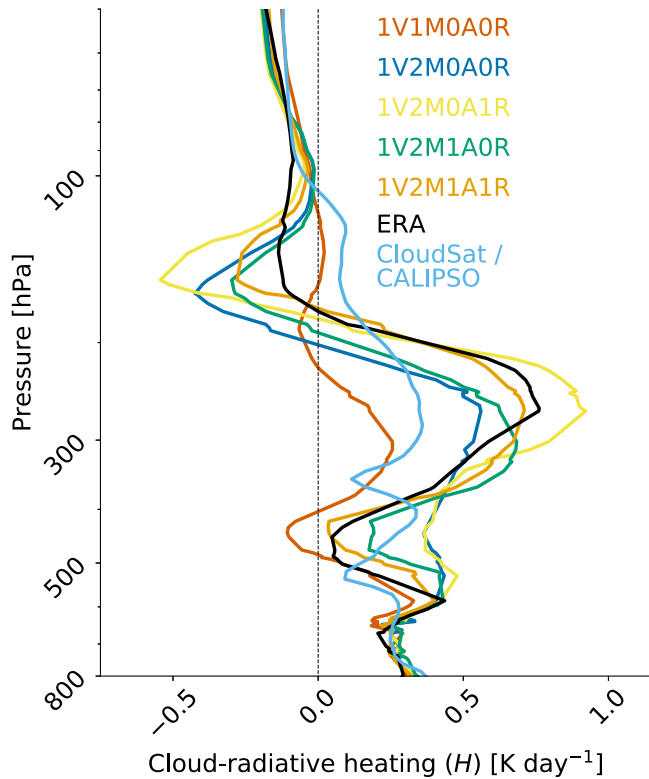


**Fig. 2 Even in convection-resolving simulations, we can generate a wide range of  $\mathcal{H}$  profiles by adjusting ice microphysical parameters.** Simulated cloud-radiative heating rate profiles, averaged over the simulation domain of Fig. 1b and with the median value taken between 7 August 2017 12:00 UTC and 8 August 2017 12:00 UTC (simulation acronyms detailed in Methods and Table S1). **1V** simulations with higher vertical resolution are shown here in the solid lines. We also show ERA5 reanalysis values over the domain for 7 and 8 August 2017 at 1°-resolution, as well as the 2B-FLXHR-LIDAR data from CloudSat/CALIPSO as in Fig. 1a. **0V** simulations with the default vertical resolution are shown as well in dashed lined in Fig. S1.

but crystal number dependence should be incorporated when we switch to the two-moment microphysics for consistency (“Methods”).

In these very high-resolution simulations, maximum  $\mathcal{H}$  still varies by a factor of four (Fig. 2). Among the modified parameters, vertical resolution has the smallest impact (**0V** versus **1V**, Fig. S1). Another nonhydrostatic icosahedral model, NICAM, showed similarly limited vertical resolution sensitivity below a certain threshold: In 14-km global simulations, the transition from a maximum vertical spacing of 400-m down to a maximum spacing of 200-m had little impact<sup>23</sup>. The inclusion of aerosol-ice interactions has a limited impact between 200 and 300 hPa (**1A**), where ice formation occurs by homogeneous nucleation. But outside of this altitudinal range, aerosol dependence reduces radiative heating and cooling values by a factor of two.

The most dramatic difference comes from switching between one- and two-moment microphysics (**1M** versus **2M**), which increases the in-cloud heating by a factor of two and the cloud-top cooling by a factor of four and produces a much more pronounced diurnal cycle in shortwave cloud heating (Fig. S2). Ice crystal effective radius consistency (**0R** versus **1R**) stretches the heating-cooling dipole by another factor of two, whereas the combination of consistent effective radius and aerosol dependence (**1A1R**) tempers this amplification somewhat and brings  $\mathcal{H}$  into the best agreement with ERA5. Thus, with ice microphysical “switches”, we can generate very distinct  $\mathcal{H}$  profiles, but none

agree even qualitatively with that from the CloudSat/CALIPSO data. We proceed by digging into the ice microphysics schemes to understand why we see such strong changes of  $\mathcal{H}$  in these high-resolution simulations.

**Microphysical explanations.** The dominant reason for greater  $\mathcal{H}$  in the two-moment versus one-moment scheme is a considerable increase in the ice mass mixing ratio ( $q_i$ , Fig. 3a). Not only does column-integrated ice mass increase by an order of magnitude (Fig. S3a), non-negligible ice mass mixing ratio extends over a larger vertical depth and to a higher altitude in the two-moment scheme relative to the one-moment one. Assuming that the infrared (longwave) component of  $\mathcal{H}$  dominates in the atmosphere and that this longwave component is in turn determined primarily by ice cloud emissivity ( $\varepsilon_i$ )<sup>12</sup>, an approximate scaling reproduces the two-fold increase in  $\mathcal{H}$ :

$$\begin{aligned} \mathcal{H}_{2M} &\sim \varepsilon_{i,2M} \sim \frac{1 - \exp\left[-\kappa_{i,2M} \int \rho_{i,2M} dz'\right]}{-\kappa_{i,2M} \int \rho_{i,2M} dz'} \\ \mathcal{H}_{1M} &\sim \varepsilon_{i,1M} \sim \frac{1 - \exp\left[-\kappa_{i,1M} \int \rho_{i,1M} dz'\right]}{-\kappa_{i,1M} \int \rho_{i,1M} dz'} \end{aligned} \quad (1)$$

$$= \frac{1 - \exp(-100 \text{ m}^2 \text{ kg}^{-1} \cdot 0.08 \text{ kg m}^{-2})}{1 - \exp(-100 \text{ m}^2 \text{ kg}^{-1} \cdot 0.008 \text{ kg m}^{-2})} \sim 2$$

where  $\kappa_i$  is the absorption cross section of ice (Fig. S3b) and  $\rho_i$  is the mass of ice absorbers per volume air, or the ice water path when integrated vertically (see mean values indicated in Fig. S3a). Along with a higher mean ice water path, the two-moment scheme generates a bimodal ice water path distribution, similar to what is seen in the 2C-ICE satellite product over the Asian monsoon region<sup>24</sup>. This ice water path bimodality has recently been attributed to separate signatures of thin cirrus versus convective outflow using the raDAR-liDAR (DARDAR) satellite product over the Indian Ocean and West Pacific<sup>25</sup>. Greater convective outflow from the two-moment scheme is consistent with its positive  $\mathcal{H}$  throughout much of the troposphere.

We next decompose why the two-moment microphysics scheme produces so much more ice, starting around 500 hPa at the warmest subzero temperatures, where ice formation occurs by *heterogeneous nucleation*. In both the default one- and two-moment schemes, heterogeneous nucleation is described by an exponential function of temperature:

$$C_{\text{INP}} = A \exp[-B(T - T_{\text{min}})^C] \quad (2)$$

where  $C_{\text{INP}}$  is the concentration of ice-nucleating particles and  $T_{\text{min}}$  is the minimum temperature for which heterogeneous nucleation can occur. In the one-moment scheme,  $C_{\text{INP}}$  is multiplied by a fixed initial crystal mass of  $10^{-12}$  kg and divided by the time step to generate an ice mass tendency from nucleation. Experimental data cannot easily constrain this relationship because ice-nucleating particle concentrations vary greatly from one region to another<sup>26</sup>. Whereas both the  $B$  and  $C$  parameters do not vary much between the two schemes (values of 0.2–0.2813 and 1–1.2873 respectively), the leading coefficient,  $A$ , varies strongly between the two microphysics schemes with a value of  $1.0 \times 10^2 \text{ m}^{-3}$  for the one-moment scheme and a value of  $2.969 \times 10^4 \text{ m}^{-3}$  for the two-moment scheme in boreal summer<sup>27,28</sup>. When we run a two-moment simulation with the one-moment value of  $A$  in the ‘A test’ simulation (black dotted trace, Fig. 3a), ice mass mixing ratios between 400 and 500 hPa correspond between the two schemes. This single parameter determines ice formation and  $\mathcal{H}$  at the warmest subzero temperatures.

The inability to constrain a temperature-dependent formulation like Eq. (2), particularly its leading coefficient, highlights the need to include the aerosol dependence of heterogeneous nucleation. When we include such dependence in the **1A**

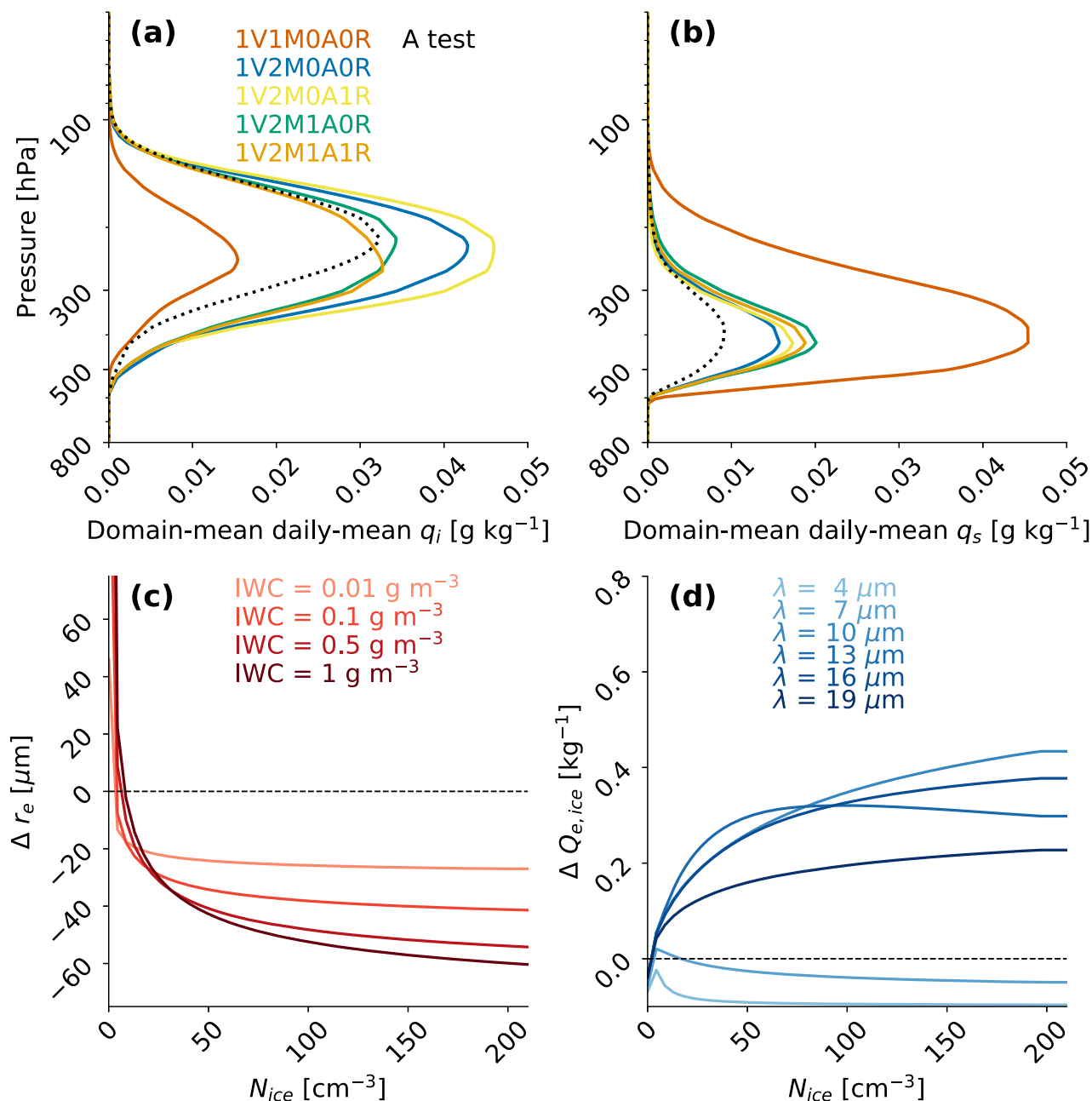


**Fig. 3 The one-moment microphysics produces far more radiatively inactive snow, the two-moment far more radiatively active ice.** A consistent treatment of effective radius also translates to higher extinction efficiencies, and hence heating, across the infrared window. Vertical profiles of domain-mean daily-mean ice and snow mass mixing ratio for the simulations, calculated over grid cells both with and without ice cloud (**a** and **b**, acronyms in Table S1). Changes in ice crystal effective radius between the default and microphysics-radiation consistent treatments, calculated offline for four fixed values of ice water content and across a range of ice crystal number concentrations (**c**). Changes in extinction efficiency per crystal mass between the default and microphysics-radiation consistent treatments throughout the infrared window for an ice water content of  $0.01 \text{ g m}^{-3}$  (**d**).

simulations (see Eq. (5) for this formulation), both cloud-top cooling above 200 hPa and in-cloud heating around 500 hPa are reduced as the column-integrated cloud condensate decreases (Fig. 2). Lower cloud-top cooling is driven by less ice crystal formation with the additional criterion of ice-nucleating aerosol present, and lower in-cloud heating is driven by less liquid cloud mass mixing ratio there (Figs. 3a and S5). These adjustments bring  $\mathcal{H}$  into better agreement with that of ERA5.

Once initial ice forms at the warmest subzero temperatures, it undergoes other processes including ice-to-snow conversion, or *ice autoconversion*, in which multiple crystals collide to form slowly precipitating aggregates. Here, the one- and

two-moment formulations diverge. In the one-moment scheme, ice is converted to snow above a threshold ice mass mixing ratio  $q_{i,0}$  at a fixed rate  $C_{\text{au}}$  of  $10^3 \text{ s}^{-1}$ :  $\partial m_s / \partial t = C_{\text{au}}(q_i - q_{i,0})^{27}$ . In contrast, the two-moment scheme uses collisional kernels between two hydrometeors to evaluate integrals over the gamma size distributions of these hydrometeors. For example, for a collision between two ice crystals to produce a snow particle, the mass mixing ratio tendencies of ice and snow are

$$\frac{\partial q_i}{\partial t} \propto -E_{ii} N_{\text{ice}} q_i G_1(\delta_i, \theta_i) \quad (3)$$



$$\frac{\partial q_s}{\partial t} = -\frac{\partial q_i}{\partial t} \tag{4}$$

where  $E_{ii}$  is the ice–ice collision efficiency,  $N_{ice}$  is the number density of ice crystals,  $q_i$  is their mass density, and  $G_1$  is a function of  $\delta_i$  and  $\theta_i$ , non-dimensional combinations of gamma distribution parameters<sup>29</sup>. The simple treatment of the one-moment scheme generates a very large amount of snow, which is radiatively inactive in ICON although not in reality, and reduces  $\mathcal{H}$  in our one-moment simulations (Fig. 3b). The more sophisticated representation of the two-moment scheme substantially limits the production of radiatively inactive snow and  $\mathcal{H}$  is correspondingly much larger. Other studies have also documented 10–25% changes in  $\mathcal{H}$  values with and without radiatively inactive snow, both in CloudSat/CALIPSO data and model intercomparison output<sup>30,31</sup>.

At the coldest temperatures with non-negligible water vapor, ice forms by *homogeneous nucleation*, a stochastic process whose rate coefficient depends strongly on the water vapor density excess, or supersaturation. Supersaturation increases as an air parcel expands adiabatically in the atmosphere, so that a direct link exists between the homogeneous nucleation tendency and vertical velocity. Constructing these vertical velocity profiles, we find that ascent rate is 20% larger in its mean value and 5% in its 99th percentile for the two-moment simulations relative to the one-moment ones (Fig. S4). Larger supersaturations can form with this stronger ascent, amplifying the homogeneous nucleation rate and ice production in the uppermost troposphere.

We turn lastly to the simulations with consistent treatment of effective radius (1R, Eqs. (6) and (7)). Ice mass mixing ratio increases further in these simulations relative to the default two-moment ones. But looking at Eq. (1), as ice water path ( $\int \rho_i dz'$ ) increases, the exponentials decay, and the ratio of heating rates approaches one.  $\mathcal{H}$  increases in this case instead because of smaller ice crystal sizes and larger ice extinction efficiencies per crystal mass ( $Q_{e,ice}$ , Fig. 3c, d). For a fixed ice water content (IWC), ice crystal effective radius decreases in its number- and

mass-dependent formulation relative to the mass-only-dependent one for almost all values of ice crystal number concentration. The higher the IWC, the larger this decrease in effective radius. These smaller crystals attenuate radiation more effectively, especially for wavelengths in the terrestrial infrared window (8–14  $\mu\text{m}$ ), where ice is orders of magnitude more absorptive than water vapor (Fig. S3b). Whether by direct absorption or absorption after multiple scattering events then,  $\mathcal{H}$  increases over most of the ice crystal number-IWC space when effective radius is consistent between the microphysics and radiation schemes.

Although we have focused on cloud ice above, cloud liquid also exists in the supercooled form up to 300 hPa and can both determine and be determined by  $\mathcal{H}$ . Low-level clouds have a higher liquid mass mixing ratio in the one-moment scheme than the two-moment scheme (Fig. S5). These optically thicker liquid clouds reemit somewhat less longwave radiation than the surface and could contribute to the reduced  $\mathcal{H}$  in the one-moment scheme. Smaller cloud liquid mass mixing ratios in the two-moment aerosol-dependent simulations explain their reduced heating between 450 and 300 hPa relative to the aerosol-independent simulations as well, in spite of equivalent ice mass mixing ratios at these altitudes. Upper-level  $\mathcal{H}$  could also feedback on low cloud formation, for example via inhibition of infrared cooling from boundary-layer cloud or through column stabilization and boundary-layer deepening, but we have not investigated whether these mechanisms are active in our simulations<sup>32,33</sup>.

**Spatial fields of outgoing longwave radiation.** Spatial fields of daily-mean outgoing longwave radiation (OLR) provide a second illustration of how the ice microphysical formulations discussed above can drastically change radiative outputs, even in storm-resolving setups. Averaged between 7 August 2017 12:00 UTC and 8 August 2017 12:00 UTC, we show OLR over our simulation domain from the CERES SYN1deg-3Hour satellite product, the ERA5 reanalysis, and five of our simulations (Fig. 4). The magnitudes and distribution of OLR vary strongly between the observations and the model and between different simulations. CERES and ERA5 both show more clear sky than any of the

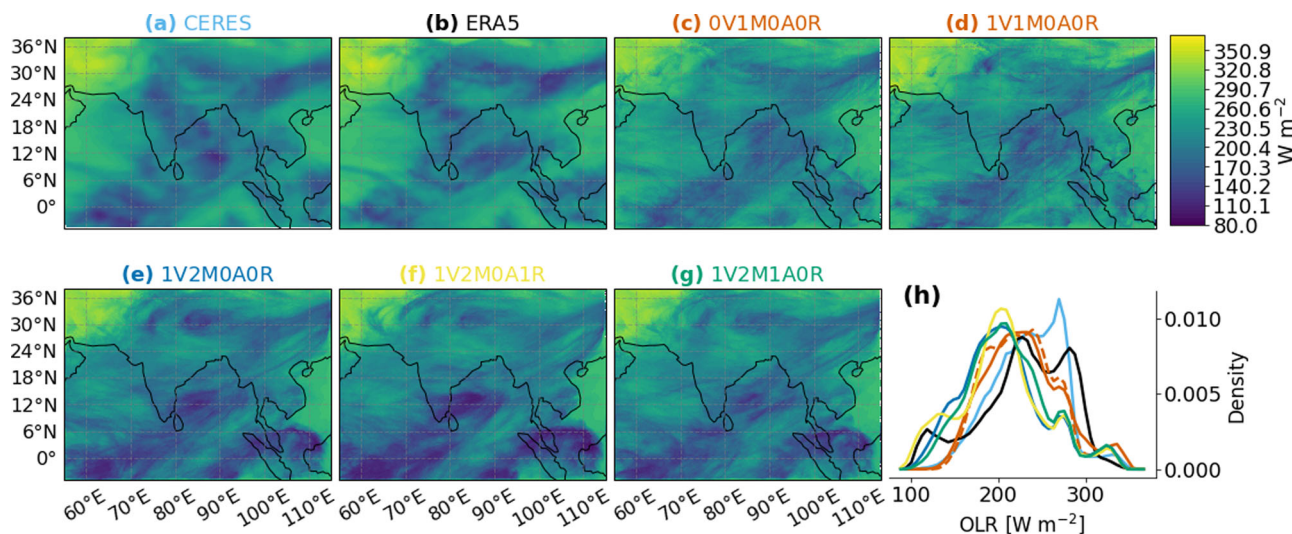


**Fig. 4 The domain-mean daily-mean outgoing longwave radiation can vary by 25 to 30  $\text{W m}^{-2}$  between satellite data, reanalysis, and high-resolution simulations.** Mean outgoing longwave radiation (OLR) between 7 August 2017 12:00 UTC and 8 August 2017 12:00 UTC from the CERES SYN1deg-3Hour product at  $1^\circ$  resolution (a), ERA5 reanalysis at  $1^\circ$  resolution (b), and five ICON simulations detailed (c–g acronyms in Table S1). Probability density distribution of OLR values from these different sources (h). Fifty bins between 80 and 375  $\text{W m}^{-2}$  are used with a three-point running mean. Color corresponds to source as in the other panel labels, with the default vertical resolution in the dashed vermillion and increased vertical resolution in solid vermillion.

model simulations (black and gray traces in Fig. 4h). Among the simulations, we see limited impact of the vertical resolution, as for  $\mathcal{H}$  (Fig. 4c, d, vermillion traces in Fig. 4h). The median OLR changes by less than  $2 \text{ W m}^{-2}$  between default and increased vertical resolution. The switch from one- to two-moment microphysics, however, shifts the OLR distribution toward much lower values, as shown by the clustering of blue and yellow traces in Fig. 4h. Median OLR drops by 25–30  $\text{W m}^{-2}$  in the two-moment simulations relative to the one-moment one. Non-negligible ice mass mixing ratios extend to higher altitudes in the two-moment scheme, lifting the effective emission temperature with it (Fig. 3a). But there are also differences within the various two-moment setups, especially for OLR values below  $200 \text{ W m}^{-2}$ . The simulation with consistent ice crystal effective radius exhibits a small peak around OLR of  $100 \text{ W m}^{-2}$ , while the other two-moment simulations have monotonically decreasing density for OLR below  $190 \text{ W m}^{-2}$ . While the dramatic mean OLR change between the one- and two-moment schemes is likely driven by the cloud-top temperature difference, the more subtle changes between various two-moment simulations are driven by differences in ice cloud optical thickness (Fig. 3).

## Discussion

We have shown here that, to take full advantage of very high-resolution atmospheric simulations, effort should now be directed toward improving the representation of the smallest atmospheric scales, particularly cloud ice microphysics. While increasing vertical resolution in the upper troposphere has limited impact on the simulated profile of tropical cloud-radiative heating ( $\mathcal{H}$ ), we have identified several influential microscale processes. The leading coefficient of a temperature-dependent heterogeneous nucleation scheme is unconstrained and controls  $\mathcal{H}$  at the lowest altitudes where ice cloud forms. Between about 200 and 400 hPa,  $\mathcal{H}$  is determined primarily by the conversion of ice to snow and whether snow is radiatively active. And ensuring consistency in the effective radius between microphysics and radiation schemes tends to produce much smaller crystals with larger extinction efficiencies. Combinations of these factors can alter maximum  $\mathcal{H}$  fourfold and daily-mean domain-mean OLR by almost  $30 \text{ W m}^{-2}$ . Such large sensitivities indicate that our modeling work will need to “zoom in” over coming years to constrain these microscale uncertainties.

Can we identify which ice microphysical parameters are most realistic or directions for improvement on the basis of  $\mathcal{H}$  values? Such an assessment is difficult, as even the ERA5 values and CloudSat/CALIPSO measurements involve assumptions about cloud properties (see Methods). But promisingly, simulations with two-moment microphysics, aerosol dependence, and consistent ice crystal effective radius (2MIAIR) agree best with ERA5 heating rates. While implementing crystal size consistency alone may magnify existing biases in the heterogeneous nucleation scheme, combined implementation of crystal size consistency with an aerosol-dependent nucleation scheme could improve simulated  $\mathcal{H}$ . The dramatic  $\mathcal{H}$  changes caused by snow-ice partitioning between the one- and two-moment schemes also emphasize the need either to define snow optical properties or to adopt a microphysical scheme that does not differentiate these frozen hydrometeor categories, such as the P3 scheme. Improvements in our thin cirrus observations or retrievals, for example through development of instruments with a lower minimum crystal size threshold or interarrival time algorithms, will also help to reduce uncertainty in upper-tropospheric  $\mathcal{H}$ , given the high sensitivity of ice extinction to small ice crystal numbers (Fig. 3c, d).

Microphysical evaluation could also be done on the basis of cloud class distributions:  $\mathcal{H}$  from the two-moment simulations resembles a deep convective classification with warming throughout the troposphere, whereas the one-moment simulations resemble isolated high cloud with warming over a very limited altitudinal range<sup>34</sup>. This difference, along with the stronger upper-tropospheric vertical velocities generated by the two-moment scheme (Fig. S4b), indicate that microphysical-dynamic feedbacks are at play. These should be the focus of future work in order to quantify how much uncertainty in cloud ice processes affects the large scale directly versus indirectly.

Ice crystal complexity and secondary ice production are other interesting factors to explore. Despite the variety of ice crystal geometries forming in the atmosphere, tabulated scattering properties within ICON are based upon Mie theory and hence assume spherical crystals<sup>35</sup>. Not only crystal number but also shape and features like surface roughness or microfacets are relevant to generate  $\mathcal{H}$ , so efforts to quantify this crystal complexity will be crucial to provide further constraints for upper-tropospheric  $\mathcal{H}$ <sup>36</sup>. Secondary ice production processes like ice-ice collisional breakup or frozen droplet shattering are also receiving increasing attention but not currently implemented in ICON. We expect that their inclusion would be similar to that of the consistent effective radius alone: The formation of many smaller crystals between 500 and 380 hPa (270 and 258 K) would increase the extinction coefficient and  $\mathcal{H}$  there. Less clear is whether the occurrence frequency of these processes would be high enough to influence  $\mathcal{H}$ , motivating future efforts to test these processes in high-resolution models.

Other relevant questions are whether and how a fourfold increase in  $\mathcal{H}$  impacts the reliability of model projections of circulation responses to warming, and hence of regional climate change. As noted above, variations in tropical  $\mathcal{H}$  partially determine the poleward shift and intensification of the Northern Hemisphere jet, as well as the poleward expansion of the meridional overturning, with global warming<sup>16,18,37</sup>. The magnitude of these circulation changes have important implications for European climate in the upcoming decades. More locally, over our simulation domain, monsoon circulations are the result of regional forcing and hence susceptible to temperature-related changes in moist static energy gradients via cloud-radiative heating<sup>38</sup>. For example, the slow-down of the Asian monsoon circulation since 1950 has been attributed to spatially inhomogeneous aerosol forcing, primarily through their indirect effect on clouds<sup>39</sup>. In idealized simulations with radiation-locking, the atmospheric cooling associated with the shortwave component of  $\mathcal{H}$  weakens the monsoon divergent flow and the cooling by clouds can expedite the monsoon onset by up to two weeks<sup>40</sup>. The ability of ice microphysics to modulate OLR could translate then to important delays in monsoon initiation. In the same vein, a robust anti-correlation between surface energy bias and precipitation bias has been found in atmosphere-only models over the Asian monsoon region<sup>41</sup>. Here again, climatological dry biases throughout the Asian monsoon region could be traced back to flaws in ice microphysical representation.

In summary, we have established a strong control of microscale ice processes on the tropical radiative energy budget. This control operates even in the new generation of storm-resolving models that will drive atmospheric science efforts in the years ahead. Our results identify a clear need to bound simulated cloud-radiative heating rates and indicate that headway can be made by first constraining cloud ice microphysics. With the deep convection problem now obviated by explicit computation, progress in our ability to model global circulation can be made by focusing on cloud microphysics and cloud-radiative interactions at the smallest atmospheric scales.

## Methods

**Model setup.** The ICON Model version 2.3.0 is run between 5 August 2017 12:00 UTC and 9 August 2017 00:00 UTC at 2.5-km-equivalent horizontal resolution (R2B10 icosahedral grid) and with a 24-s time step. At this spatial resolution, we resolve deep convection but parameterize shallow convection with the Nordeng scheme<sup>42</sup>. 2D fields are output every half hour and 3D fields every hour. Cloud-radiative heating is calculated as the difference of all-sky and clear-sky flux divergences. The domain extends over the Asian monsoon region from 55°E to 115°E and 5°S to 40°N (Fig. 1b). ICON employs a hybrid sigma height grid vertically with 75 levels by default (Fig. 1c). Simulations using this default resolution are denoted **0V**. In some simulations, we employ 120 levels by enforcing a maximum layer thickness of 200 m below 17 km, and these are denoted **1V** (Table S1). Initial and lateral boundary conditions come from the Integrated Forecast System (IFS) analysis data of the European Center for Medium-Range Weather Forecast (ECMWF). We use the IFS boundary data every 3 h, analysis values at 0000 and 1200 UTC and forecast values in between. Surface and aerosol data come from the German Weather Service (DWD).

**Model physics.** We use both the one-moment microphysics described in Doms et al.<sup>27</sup> and the two-moment microphysics of Seifert and Beheng<sup>29</sup> (denoted **1M** and **2M** respectively throughout, Table S1). In the default two-moment scheme, parameters for the ice nucleation and droplet activation spectra come from Hande et al.<sup>28</sup>. We also run simulations with the Phillips et al.<sup>43</sup> ice nucleation parameterization (denoted **1A** throughout, Table S1) and climatological, not prognostic, aerosol. Phillips et al.<sup>43</sup> calculate the number of ice-nucleating particles ( $n_{\text{INP}}$ ) in three aerosol groups—dust and metallics, black carbon, and organics—as follows:

$$n_{\text{INP},X} = \int_{\log 0.1\mu\text{m}}^{\infty} \{1 - \exp[-\mu_X(D, S_i, T)]\} n_X(\log D) d \log D \quad (5)$$

where  $\mu_X$  represents the number of ice embryos forming per aerosol and  $n_X(\log D)$  is the aerosol size distribution. We use the warm-rain parameterization of Seifert and Beheng<sup>44</sup>, the Rapid Radiative-Transfer Model (RRTM), and the Tegen aerosol climatology<sup>45,46</sup>. Trace gas mixing ratios are set to the annual global means from the input4MIPS project (390 ppm CO<sub>2</sub>, 1800 ppb CH<sub>4</sub>, 322 ppb N<sub>2</sub>O, 240 ppt CFC11, 532 ppt CFC12), except for O<sub>3</sub> which comes from the GEMS climatology. Mie theory is used to calculate cloud optical properties, assuming sphericity and lognormal size distributions.

**Consistency in the ice crystal effective radius.** In the default model setup, ice crystal effective radius depends solely on ice mass mixing ratio, making it inconsistent with the two-moment microphysics<sup>35,47</sup>:

$$r_{\text{ei}} = 83.8 q_i^{0.216} \quad (6)$$

We make this effective radius calculation consistent with the two-moment microphysics, as in Appendix B of Kretzschmar et al.<sup>47</sup>. Ice crystal effective radius is evaluated from the ratio of the third to second moment of the generalized gamma distribution for hydrometeor sizes from Seifert and Beheng<sup>29</sup>:

$$r_{\text{ei}} = \frac{a}{2} \left[ \frac{L_i}{N_i} \frac{\Gamma(\frac{\nu+1}{\mu})}{\Gamma(\frac{\nu+2}{\mu})} \right]^b \frac{\Gamma(\frac{3b+\nu+1}{\mu})}{\Gamma(\frac{2b+\nu+1}{\mu})} \quad (7)$$

where  $a$  and  $b$  are the leading coefficient and exponent in a mass-dimension power law;  $L_i$  and  $N_i$  are the column-integrated ice mass and the ice crystal number concentration respectively; and  $\mu$  and  $\nu$  are parameters of the gamma distribution. For a cloud with IWC of 0.01 g m<sup>-3</sup> and an ice crystal number concentration of 100 cm<sup>-3</sup>, effective radius decreases by 80% with this new formulation relative to the old.

**Satellite and reanalysis data and 'CMIP-like' simulations.** We compare our modeled radiative fields with those from the ERA5 reanalysis of the ECMWF<sup>48</sup>. ERA5 assimilates radiances from both infrared sounders like AIRS and IASI and from geostationary satellites like the GOES and Meteosat series, while the underlying IFS employs the RRTM, liquid optical thickness dependent on liquid water path and cloud condensation nuclei concentrations, and a temperature-dependent ice crystal effective radius<sup>48</sup>. Shortwave and longwave clear-sky and all-sky fluxes are downloaded at 1° resolution from 5 to 9 August 2017 in the simulation domain. 2B-FLXHR-LIDAR data, version P2R04 are used from CloudSat/CALIPSO data at 2.5° resolution over the simulation domain from 2006 to 2011<sup>49</sup>. 2B-FLXHR-LIDAR heating rates are retrieved using CloudSat cloud profiling radar measurements of liquid and IWCs and supplemented by CALIPSO and Moderate Resolution Imaging Spectroradiometer measurements as necessary. The retrieval also employs a two-stream radiative-transfer approximation and the CloudSat ECMWF-AUX auxiliary product. OLR observations over the simulation domain from 5–9 August 2019 are downloaded from the CERES SYN1deg-3Hour product. Comparisons are also made to coarse-resolution output of the atmospheric component of the MPI-ESM model, the atmospheric component LMDz5A of the IPSL-CM5A model, and version 2.1.00 of ICON at R2B04 (160 km resolution) with climatological sea surface temperature throughout the tropics (see Voigt et al.<sup>18</sup>

Section 4 for more details). These simulations have spatial resolution of roughly 150 km, and we calculate  $\mathcal{H}$  from monthly mean model output over 5 or more years. We understand these  $\mathcal{H}$  values as a tropical climatology from models equivalent to those in the CMIP.

## Data availability

Postprocessed model output is available at <https://doi.org/10.5281/zenodo.4808394><sup>50</sup>. CERES SYN1deg data can be downloaded from <https://ceres.larc.nasa.gov/products.php?product=SYN1deg>, and ERA5 reanalysis values are available at <https://www.ecmwf.int/en/forecasts/datasets/reanalysis-datasets/era5>. We thank NASA and the ECMWF for making these data publicly available.

## Code availability

All codes to reproduce figures from postprocessed output are available at [https://github.com/sylviasullivan/icon\\_2.3.0\\_ice-mp\\_rad\\_vis](https://github.com/sylviasullivan/icon_2.3.0_ice-mp_rad_vis).

Received: 5 April 2021; Accepted: 9 June 2021;

Published online: 01 July 2021

## References

- Satoh, M. et al. Global cloud-resolving models. *Curr. Clim. Change Rep.* **5**, 172–184 (2019).
- Wedi, N. P. et al. A baseline for global weather and climate simulations at 1-km resolution. *J. Adv. Model. Earth Sys.* **12**, <https://doi.org/10.1029/2020MS002192> (2020).
- Stevens, B. et al. DYAMOND: the DYnamics of the Atmospheric general circulation Modeled On Non-hydrostatic Domains. *Prog. Earth Planet. Sci.* **6**, <https://doi.org/10.1186/s40645-019-0304-z> (2019).
- Stevens, B. et al. The added value of large-eddy and storm-resolving models for simulating clouds and precipitation. *J. Meteorol. Soc. Jap.* **98**, 395–435 (2020).
- Sullivan, S. C., Betancourt, R. M., Barahon, D. & Nenes, A. Understanding cirrus ice crystal number variability for different heterogeneous ice nucleation spectra. *Atmos. Chem. Phys.* **16**, 2611–2629 (2015).
- Fan, J., Wang, Y., Rosenfeld, D. & Liu, X. Review of aerosol-cloud interactions: Mechanisms, significance, and challenges. *J. Atmos. Sci.* **73**, 4221–4252 (2016).
- Lawson, R. P. et al. A review of ice particle shapes in cirrus formed in-situ and in anvils. *J. Geophys. Res.* **124**, 10049–10090 (2019).
- Sherwood, S. C. et al. An assessment of Earth's climate sensitivity using multiple lines of evidence. *Rev. Geophys.* **58**, <https://doi.org/10.1029/2019RG000678> (2020).
- Randel, W. J. et al. Asian monsoon transport of pollution to the stratosphere. *Science* **328**, <https://doi.org/10.1126/science.1182274> (2010).
- Lelieveld, J. et al. The South Asian monsoon—pollution pump and purifier. *Science* **361**, 270–273 (2018).
- Kuhn, P. M. & Weickmann, H. K. Light scattering by ice clouds in the visible and infrared: a theoretical study. *J. Atmos. Sci.* **29**, 524–536 (1972).
- Fleming, J. R. & Cox, S. K. Radiative effects of cirrus clouds. *J. Atmos. Sci.* **31**, 2182–2188 (1974).
- Nazaryan, H., McCormick, M. P. & Menzel, W. P. Global characterization of cirrus clouds using CALIPSO data. *J. Geophys. Res.* **113**, <https://doi.org/10.1029/2007JD009481> (2008).
- Li, Y., Thompson, D. W. J. & Bony, S. The influence of atmospheric cloud radiative effects on the large-scale circulation. *J. Clim.* **28**, 7263–7278 (2015).
- Albern, N., Voigt, A., Buehler, S. A. & Grützun, V. Robust and nonrobust impacts of atmospheric cloud-radiative interactions on the tropical circulation and its response to surface warming. *Geophys. Res. Lett.* **45**, 8577–8585 (2018).
- Voigt, A. et al. Clouds, radiation, and atmospheric circulation in the present-day climate and under climate change. *WIREs Clim Change*, 12:e694 (2021).
- Shaw, T. A. Mechanisms of future predicted changes in the zonal mean mid-latitude circulation. *Curr. Clim. Change Rep.* **5**, 345–357 (2019).
- Voigt, A., Albern, N. & Papavasiliou, G. The atmospheric pathway of the cloud-radiative impact on the circulation response to global warming: Important and uncertain. *J. Clim.* **32**, 3051–3067 (2019).
- Li, J.-L., Thompson, D. W. J., Bony, S. & Merlis, T. M. Thermodynamic control on the poleward shift of the extratropical jet in climate change simulations: The role of rising high clouds and their radiative effects. *J. Clim.* **32**, 917–934 (2019).
- Cesana, G. et al. The vertical structure of radiative heating rates: a multimodel evaluation using A-Train satellite observations. *J. Clim.* **32**, 1573–1590 (2019).
- Sullivan, S. C., Lee, D., Oreopoulos, L. & Nenes, A. The role of updraft velocity in temporal variability of global cloud hydrometeor number. *Proc. Natl Acad. Sci. USA* **113**, 5791–5796 (2016).



22. Barahona, D., Molod, A. & Kalesse, H. Direct estimation of the global distribution of vertical velocity within cirrus clouds. *Sci. Rep.* **7**, <https://doi.org/10.1038/s41598-017-07038-6> (2017).
23. Seiki, T. et al. Vertical grid spacing necessary for simulating tropical cirrus clouds with a high-resolution atmospheric general circulation model. *Geophys. Res. Lett.* **42**, 4150–4157 (2015).
24. Berry, E. & Mace, G. G. Cloud properties and radiative effects of the Asian summer monsoon derived from A-Train data. *J. Geophys. Res. Atmos.* **119**, 9492–9508 (2014).
25. Sokol, A. B. & Hartmann, D. L. Tropical anvil clouds: radiative driving toward a preferred state. *J. Geophys. Res.: Atm.* **125**, <https://doi.org/10.1002/essoar.10503124.1> (2020).
26. DeMott, P. J. et al. Predicting global atmospheric ice nuclei distributions and their impacts on climate. *Proc. Nat. Acad. Sci. USA* **107**, 11217–11222 (2011).
27. Doms, G. et al. *A Description of the Nonhydrostatic Regional Model LM*. Tech. Rep. (Deutscher Wetterdienst, 2005).
28. Hande, L., Engler, C., Hoose, C. & Tegen, I. Seasonal variability of Saharan desert dust and ice nucleation particles over Europe. *Atmos. Chem. Phys.* **15**, 4389–4397 (2015).
29. Seifert, A. & Beheng, K. D. A two-moment cloud microphysics parameterization for mixed-phase clouds. Part I: Model description. *Meteorol. Atmos. Phys.* **92**, 45–66 (2006).
30. Waliser, D. E., Li, J.-L. F., L'Ecuyer, T. S. & Chen, W.-T. The impact of precipitation ice and snow on the radiation balance in global climate models. *Geophys. Res. Lett.* **38**, <https://doi.org/10.1029/2010GL046478> (2011).
31. Li, J.-L. et al. Considering the radiative effects of snow on tropical Pacific Ocean radiative heating profiles in contemporary GCMs using A-Train observations. *J. Geophys. Res.: Atm.* **121**, 1621–1636 (2016).
32. Masunaga, H. & Bony, S. Radiative invigoration of tropical convection by preceding cirrus clouds. *J. Atm. Sci.* **75**, 1327–1342 (2018).
33. Bretherton, C. Insights into low-latitude cloud feedbacks from high-resolution models. *Philos. Trans. R. Soc. A* **373**, <https://doi.org/10.1098/rsta.2014.0415> (2015).
34. Johansson, E., Devasthale, A., L'Ecuyer, T., Ekman, A. M. L. & Tjernström, M. The vertical structure of cloud radiative heating over the Indian subcontinent during summer monsoon. *Atmos. Chem. Phys.* **15**, 11557–11570 (2015).
35. Stevens, B. et al. Atmospheric component of the MPI-M Earth System Model: ECHAM6. *J. Adv. Model. Earth Syst.* **5**, 146–172 (2013).
36. Järvinen, E. et al. Additional global climate cooling by clouds due to ice crystal complexity. *Atmos. Chem. Phys.* **18**, 15767–15781 (2018).
37. Albern, N., Voigt, A., Thompson, D. W. J. & Pinto, J. G. The role of tropical, midlatitude, and polar cloud-radiative changes for the midlatitude circulation response to global warming. *J. Clim.* **33**, 7927–7943 (2020).
38. Biasutti, M. et al. Global energetics and local physics as drivers of past, present and future monsoons. *Nat. Geosci.* **11**, 392–400 (2016).
39. Bollasina, M., Ming, Y. & Ramaswamy, V. Anthropogenic aerosols and the weakening of the South Asian summer monsoon. *Sci.* **334**, 502–505 (2011).
40. Byrne, M. & Zanna, L. Radiative effects of clouds and water vapor on an axisymmetric monsoon. *J. Clim.* **33**, 8789–8811 (2020).
41. Yang, B. et al. Better monsoon precipitation in coupled climate models due to bias compensation. *npj Clim. Atmos. Sci.* **2**, <https://doi.org/10.1038/s41612-019-0100-x> (2019).
42. Nordeng, T. E. Extended versions of the convective parametrization scheme at ECMWF and their impact on the mean and transient activity of the model in the tropics. Tech. Rep. (ECMWF Tech. Memo., Shinfield Park, Reading, 1994).
43. Phillips, V. T. J., DeMott, P. J. & Andronache, C. An empirical parameterization of heterogeneous ice nucleation for multiple chemical species of aerosol. *J. Atm. Sci.* **65**, 2757–2783 (2008).
44. Seifert, A. & Beheng, K. D. A double-moment parameterization for simulating autoconversion, accretion and self collection. *Atmos. Res.* **59–60**, 265–281 (2001).
45. Mlawer, E. J., Taubman, S. J., Brown, P. D., Iacono, M. J. & Clough, S. A. Radiative transfer for inhomogeneous atmospheres: RRTM, a validated correlated-k model for the longwave. *J. Geophys. Res.* **102**, 16663–16682 (1997).
46. Tegen, I. et al. Contribution of different aerosol species to the global aerosol extinction optical thickness: estimates from model results. *J. Geophys. Res.* **102**, 23895–23915 (1997).
47. Kretzschmar, J., Stapf, J., Klocke, D., Wendisch, M. & Quaas, J. Employing airborne radiation and cloud microphysics observations to improve cloud representation in ICON at kilometer-scale resolution in the Arctic. *Atmos. Chem. Phys.* **20**, 13145–13165 (2020).
48. Hersbach, H. et al. The ERA5 global reanalysis. *Q. J. Roy. Meteorol. Soc.* **146**, 1999–2049 (2020).
49. L'Ecuyer, T. S., Wood, N. B., Haladay, T., Stephens, G. L. & Stackhouse, P. W. Impact of clouds on atmospheric heating based on the R04 CloudSat fluxes and heating rates data set. *J. Geophys. Res.* **113**, <https://doi.org/10.1029/2008JD009951> (2008).
50. Sullivan, S. Postprocessed cloud radiative and microphysical output - ICON model <https://doi.org/10.5281/zenodo.4808394> (2021).

## Acknowledgements

S.C.S. was funded by DFG project VO 1765/6-1 (TropiC). A.V. received funding from the German Ministry of Education and Research (BMBF) and FONA: Research for Sustainable Development (www.fona.de) under grant 01LK1509A. Simulations were run on the mistral supercomputer of the German Climate Computation Center (DKRZ), and we gratefully acknowledge DKRZ technical support. Many thanks to Jan Kretzschmar for sharing his implementation of microphysical-radiative consistency for effective radius in the ICON model, as well as for providing verification of Fig. 3c, and to Odran Sourdeval for bringing the effective radius inconsistency to our attention. We acknowledge Georgios Papavasileiou for preparing the CloudSat/CALIPSO data and Nicole Albern for sharing the ICON AMIP simulations shown in Figs. 1c and 2. S.C.S. also acknowledges the CONSTRAIN working group at KIT and the larger group of researchers and students in the NSF-PIRE project 1743753, whose ideas and feedback have greatly helped this work. Finally, thanks go to two anonymous reviewers whose time and feedback have improved this manuscript.

## Author contributions

S.C.S. and A.V. conceived the study and analyzed simulation output. SS ran simulations and wrote the manuscript with assistance from AV. S.C.S. postprocessed output and generated the figures.

## Funding

Open Access funding enabled and organized by Projekt DEAL.

## Competing interests

The authors declare no competing interests.

## Additional information

**Supplementary information** The online version contains supplementary material available at <https://doi.org/10.1038/s43247-021-00206-7>.

**Correspondence** and requests for materials should be addressed to S.C.S. or A.V.

**Peer review information** Communications Earth & Environment thanks the anonymous reviewers for their contribution to the peer review of this work. Primary Handling Editors: Jan Lenaerts, Heike Langenberg. Peer reviewer reports are available.

**Reprints and permission information** is available at <http://www.nature.com/reprints>

**Publisher's note** Springer Nature remains neutral with regard to jurisdictional claims in published maps and institutional affiliations.



**Open Access** This article is licensed under a Creative Commons Attribution 4.0 International License, which permits use, sharing, adaptation, distribution and reproduction in any medium or format, as long as you give appropriate credit to the original author(s) and the source, provide a link to the Creative Commons license, and indicate if changes were made. The images or other third party material in this article are included in the article's Creative Commons license, unless indicated otherwise in a credit line to the material. If material is not included in the article's Creative Commons license and your intended use is not permitted by statutory regulation or exceeds the permitted use, you will need to obtain permission directly from the copyright holder. To view a copy of this license, visit <http://creativecommons.org/licenses/by/4.0/>.

© The Author(s) 2021